Article:
Otosaka, I orcid.org/0000-0001-9740-3735, Belmonte Rivas, M and Stoffelen, A (2018) Bayesian Sea Ice Detection With the ERS Scatterometer and Sea Ice Backscatter Model at C-Band. IEEE Transactions on Geoscience and Remote Sensing, 56 (4). pp. 2248-2254. ISSN 0196-2892

https://doi.org/10.1109/TGRS.2017.2777670

Bayesian sea ice detection with the ERS scatterometer and sea ice backscatter model at C-band

Inès Otosaka, Maria Belmonte Rivas and Ad Stoffelen

Abstract— This paper describes the adaptation of a Bayesian sea ice detection algorithm for the scatterometer on board the European Remote Sensing satellites (ERS-1 and ERS-2). The algorithm is based on statistics of distances to ocean wind and sea ice Geophysical Model Functions (GMFs) and its performance is validated against coincident active and passive microwave data. We furthermore propose a new model for sea ice backscatter at C-band in vertical polarization (VV) based on the sea ice GMFs derived from ERS and ASCAT data. The model characterizes the dependence of sea ice backscatter on incidence angle and sea ice type, allowing a more precise incidence angle correction than afforded by the usual linear transformation. The resulting agreement between the ERS, QuikSCAT and SSMI sea ice extents during the year 2000 is high during the fall and winter seasons, with an estimated ice edge accuracy of about 20 km, but shows persistent biases between scatterometer and radiometer extents during the melting period, with scatterometers being more sensitive to summer (lower concentration and rotten) sea ice types.

Index Terms— Sea ice, radar scattering, Bayes procedure, microwave radiometry

I. Introduction

SEA ice is a vital component of the cryosphere and plays an important role in global climate regulation. The heat exchanges between the atmosphere and the ocean are altered by changes in sea ice extent and thickness [1] and therefore, many concerns arise from the decline of the Arctic sea ice and the rapid loss of Arctic multi-year ice [2,3]. The operation of polar Earth observation satellites has been supporting a growing interest in the Polar Regions over the last decades, and scatterometer data have proved valuable in monitoring sea ice extent, thickness, and motion. A Bayesian algorithm for sea ice detection has been developed for QuikSCAT [4] and applied to ASCAT [5]. The focus of this paper is the adaptation of this Bayesian approach to ERS, in order to extend the existing sea ice extent scatterometer record to the ERS period (1992-2000). The resulting extended scatterometer record provides sea ice extent data over 25 years and additionally monitors the backscatter response from sea ice, which can be used to separate First-Year Ice (FYI) from Multi-Year Ice (MYI) [6]. Scatterometers collect backscatter measurements from a wide range of incidence angles (which also varies from one sensor to another) and therefore, to build a uniform record of sea ice backscatter, it is necessary to normalize sea ice backscatter to a reference angle. For this purpose, a model for sea ice backscattering at C-band in vertical polarization (VV) is developed. This model is intended for ERS and ASCAT and characterizes the dependencies of sea ice backscatter on incidence angle and sea ice type.

Section II details the original Bayesian sea ice detection algorithm for ASCAT and how it has been adapted to the ERS record. Section III reports on its validation and presents the entire scatterometer record from 1992 to 2016. Section IV details the construction of an empirical C-band sea ice backscatter model to be used as normalization tool, and as an empirical aid towards the theoretical modelling of sea ice backscatter. Section V summarizes our results and provides an overview of future work..

I. Otosaka was with the Royal Netherlands Meteorological Institute in De Bilt, The Netherlands. She is now with the Centre for Polar Observation and Modelling, School of Earth and Environment, University of Leeds, Leeds, LS2 9JT, United Kingdom (e-mail: eeino@leeds.ac.uk). M. Belmonte Rivas and A. Stoffelen are with the Royal Netherlands Meteorological Institute, De Bilt, The Netherlands (e-mails: belmonte@knmi.nl, stoffelen@knmi.nl).

II. Algorithm description

Scatterometers are active microwave sensors primarily designed for the retrieval of wind speed and direction over the ocean. They have also been used for the detection and characterization of sea ice [7]. The ERS sea ice detection algorithm proposed here is a modified version of an existing algorithm developed for ASCAT, adjusted to compensate for their different observation geometries. Both ERS and ASCAT operate at C-band (5.3 GHz) and collect triplets of VV polarized backscatter measurements $\{\sigma^0_{FORE}, \sigma^0_{MID}, \sigma^0_{AFT}\}$ from three antennas oriented at 45°, 90° and 135° relative to the flight direction (see Fig. 1). The ERS single-side antenna covers a 500-km swath divided into 25 km regular grid wind vector cells (WVCs), with incidence angles ranging from 18° to 46° for the mid-beam, and 25° to 57° for the fore and aft beams. This differs from ASCAT, which is a double-sided scatterometer with three antennas on each side covering a total swath of 1100 km also divided into 25 km grid cells. The ASCAT incidence angles are slightly larger than ERS's, as shown in Table 1.

This section provides an overview of the ASCAT algorithm followed by a description of the adjustments made for the specific geometry of ERS. A complete description of the

ASCAT algorithm can be found in [5].

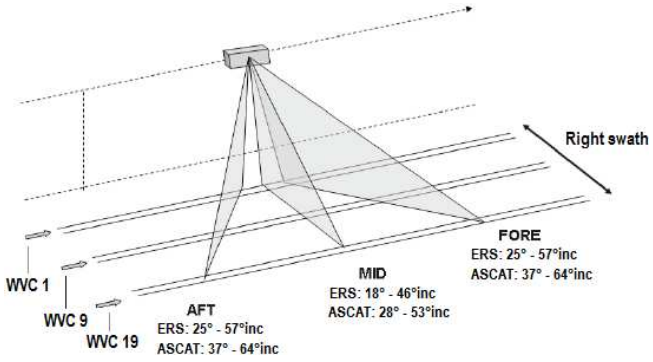

Fig. 1. Observation geometry of ERS and ASCAT (adapted from [5]).

Table 1. ERS and ASCAT observation angles for the different WVCs

ERS		ASCAT	
WVC	**Incidence mid/fore (°)**	**WVC**	**Incidence mid/fore (°)**
1	18.0 / 24.8	**1, 42**	52.4 / 63.6
2	19.8 / 27.2	**2, 41**	51.4 / 62.7
3	21.7 / 29.6	**3, 40**	50.5 / 61.8
4	23.5 / 31.8	**4, 39**	49.5 / 60.8
5	25.2 / 34.0	**5, 38**	48.5 / 59.8
6	26.9 / 36.1	**6, 37**	47.4 / 58.7
7	28.6 / 38.1	**7, 36**	46.3 / 57.6
8	30.2 / 40.0	**8, 35**	45.2 / 56.5
9	31.8 / 41.8	**9, 34**	44.1 / 55.3
10	33.4 / 43.6	**10, 33**	42.9 / 54.0
11	34.9 / 45.3	**11, 32**	41.7 / 52.8
12	36.3 / 46.9	**12, 31**	40.3 / 51.5
13	37.7 / 48.5	**13, 30**	39.1 / 50.1
14	39.1 / 49.9	**14, 29**	37.8 / 48.6
15	40.5 / 51.4	**15, 28**	36.5 / 47.1
16	41.8 / 52.8	**16, 27**	35.1 / 45.6
17	43.0 / 54.1	**17, 26**	33.6 / 43.9
18	44.2 / 55.3	**18, 25**	32.2 / 42.3
19	45.4 / 56.5	**19, 24**	30.7 / 40.5
		20, 23	29.1 / 38.7
		21, 22	27.5 / 36.8

A. The original sea ice detection algorithm for ASCAT

The original sea ice detection algorithm for ASCAT combines prior knowledge about the expected location of the sea ice edge with conditional probability functions modelled as functions of the distance of backscatter triplets to the ocean wind and sea ice Geophysical Model Functions (GMFs) [5]. Other Bayesian formulations for sea ice detection with scatterometer data can be found in the literature, such as the approach developed by Anderson and Long in [8]. The main difference lies in their use of aggregates such as mean backscatter, polarization ratio and azimuthal anisotropy as class discriminants, and empirically adjusted covariances as class dispersion. The advantage of our GMF approach is that the dispersion of measurements about extended class model functions is smaller than about class aggregate means, approaching the limits imposed by the scatterometer noise levels, and allowing the Bayesian method to reach its maximum discrimination power [4].

The ocean wind GMF, denoted CMOD7 [9], relates measured backscatter triplets, σ^0_{wind}, to wind speed v, direction ϕ, and incidence angle θ. Since θ is dependent on the across-track wind vector cell number (WVC, Table 1), we may write:

$$\sigma^0_{wind} = CMOD7(v, \phi, WVC) \quad (1)$$

The ocean wind GMF, shown on Fig. 2., conforms to a two-dimensional cone-shaped manifold in the three-dimensional measurement space formed by the scatterometer fore, mid and aft beam views [10]. The sea ice GMF, denoted the ice line (see Fig. 2), relates backscatter to sea ice type and is also WVC dependent. The distributions of stable wintertime sea ice backscatter indicate that it is azimuthally isotropic:

$$\sigma^0_{ice,FORE} = \sigma^0_{ice,AFT} \quad (2)$$

So that backscatter collected from the side beams of the same WVC is generally leveled. The relation between the backscatter collected from the mid and side beams is different, since their incidence angles differ slightly. This relation is parameterized as a one-dimensional straight line in the measurement space:

$$\sigma^0_{ice,MID} = \alpha + \beta\, \sigma^0_{ice,FORE} \quad (3)$$

The two GMFs do generally not intersect, but in the middle of the swath the ice line coincides with along-track winds and thus at the corresponding angles, the discrimination between sea ice and open ocean is left to some contextual information such as the previous passes of the satellite or Numerical Weather Prediction (NWP) model wind constraints [4,5].

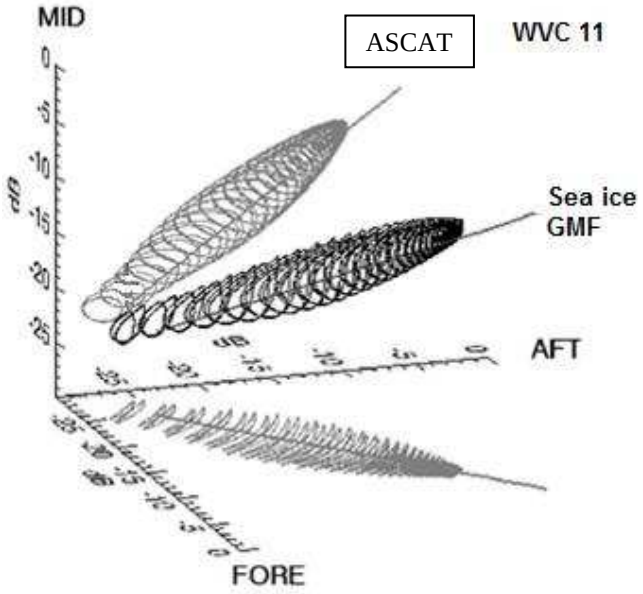

Fig. 2. Ocean wind and Sea ice GMFs at C-band (adapted from [5])

The Bayesian posterior sea ice probability is formulated as [5]:

$$p(ice|\sigma^0) = \frac{p(\sigma^0|ice)p_0(ice)}{p(\sigma^0|ice)p_0(ice) + p(\sigma^0|wind)p_0(wind)} \quad (4)$$

The conditional probability functions are expressed using Maximum Likelihood Estimates (MLEs) as normalized measures of distance from observed backscatter triplets to the ocean wind and sea ice GMFs:

$$p(\sigma^0|wind) = p(MLE_{wind}) \quad (5)$$

$$p(\sigma^0|ice) = p(MLE_{ice}) \quad (6)$$

The a-priori probabilities, $p_0(ice)$ and $p_0(wind)$, are initialized on the very first pass of the satellite as:

$$p_0(ice) = 1 - p_0(wind) = 0.35 \quad (7)$$

This initial setting is based on the climatological fraction of sea-ice to open-ocean area, and it is only used for initializing the algorithm. It does not have any significant influence on the sea ice probabilities beyond the algorithm spin-up period, which is of about 5 days.

The a-priori probabilities are updated after each orbital pass with the posteriors from the previous pass:

$$p_0(ice) = 1 - p_0(wind) = p(ice|\sigma^0) \quad (8)$$

Once a day, the posterior sea ice probability is spatially smoothed with an exponential decay function of 17 km width. Blurring the ice map is used to represent the possibility for sea ice to freeze or thaw within a day, especially near the sea ice edge.

The posterior sea ice probability is then relaxed to start as the next day prior. This relaxation is substantial and biased towards water so that the algorithm provides more reasonable probabilities in the melting marginal ice zone

$$p_0(ice) = \begin{cases} 0.50 & if\ p(ice|\sigma^0) > 0.70 \\ 0.15 & if\ p(ice|\sigma^0) < 0.70 \end{cases} \quad (9)$$

This relaxation scheme is introduced to protect the Bayesian filter from saturation (i.e., situations for which posteriors can only change slowly because the priors are too strong and do no longer reflect the true sea ice probability) and proves efficient at inhibiting weather noise caused by, e.g., rain storms or confused sea states. Please note that wind variability has been shown to cause MLE increases over high-latitude water. The rain column is generally too shallow to cause rain effects [11].

A sea ice coverage map is written once a day on a 12.5 km polar stereographic grid using a fixed 55% threshold on the posterior sea ice probability and is filled with normalized sea ice backscatter data. The 55% threshold is chosen to give the best agreement to the 15% sea ice concentration edge from passive microwave algorithms during the sea ice growth season.

B. Algorithm adjustments for ERS

ERS differs from ASCAT by its lower observation density (single 500 km swath versus double-sided 550 km swath antennas), somewhat worse noise characteristics, and slightly lower incidence angles. In order to compensate for the lower detection capabilities afforded by the narrower swath, which translates into a weaker conditioning of the priors used for sea ice detection, we introduce the following changes in the ERS sea ice processing chain:

1) The spatial smoothing is applied on an orbital basis (instead of on a daily basis) with a spatial filter width increased to 34 km, so that each grid cell collects more contextual information from nearby observations.

2) To compensate for the smaller number of ERS observations compared to ASCAT, and preserve the balance between the amount of prior and actual information used to compute the sea ice concentration, the weight of observations is doubled before the spatial filtering.

3) The fixed detection threshold of 55% is modified into using a seasonally-varying threshold on the posterior sea ice probability, lowered to 40% during the winter months (when rapid ice growth dynamics make detection more challenging, i.e., from 1st September to 1st April in the NH, and from 1st February to 1st October in the SH) and set to 50% during the rest of the year. The seasonally varying threshold scheme for ERS is chosen to provide the best agreement to the collocated sea ice edge from ASCAT/QuikSCAT all year round. The sustained lower probability thresholds required for sea ice detection with the ERS system give testimony of its limited sampling over a day.

4) Additionally, the iceline parameters (α, β) from the ASCAT sea ice GMF are extrapolated cubically to the lower incidence angles of ERS after checking that the extrapolation error, measured as the distance between the sea ice GMF derived from ERS data and the extrapolated model is less than 0.1 dB.

III. Algorithm Validation and Limitations

To validate the algorithm, a comparison with two reference data sets is performed from January through December 2000. The first reference data set is the record of sea ice extents produced from QuikSCAT data with the KNMI Bayesian sea ice detection algorithm [4]. The second dataset is the passive microwave record of sea ice extents derived from SSMI using a 15% threshold on the sea ice concentrations generated by the NASA Team NT algorithm [12].

Figure 3 shows that the agreement between the ERS and QuikSCAT sea ice extents is excellent all year long, with differences within 0.25 million km^2, and an estimated sea ice edge accuracy of 20 km. The agreement between scatterometer and SSMI sea ice extents is of comparably high quality during the fall and winter months, but degrades during spring and summer, with passive microwave (SSMI) products showing lower sensitivity to melting sea ice conditions than ERS or QuikSCAT.

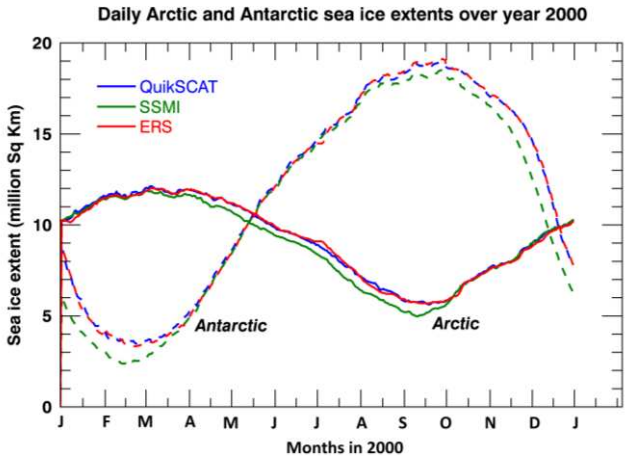

Fig. 3. Daily Arctic and Antarctic sea ice extents from Jan' 01 through Dec' 31 from ERS (red line), QuikSCAT (blue line) and SSMI (green line)

After detailed examination of the daily sea ice extents, we observe that the largest differences between the ERS and the reference QuikSCAT and SSMI records tend to occur under highly dynamic conditions (i.e., during fast sea ice advance or

retreat episodes) or during periods when no ERS observations are available.

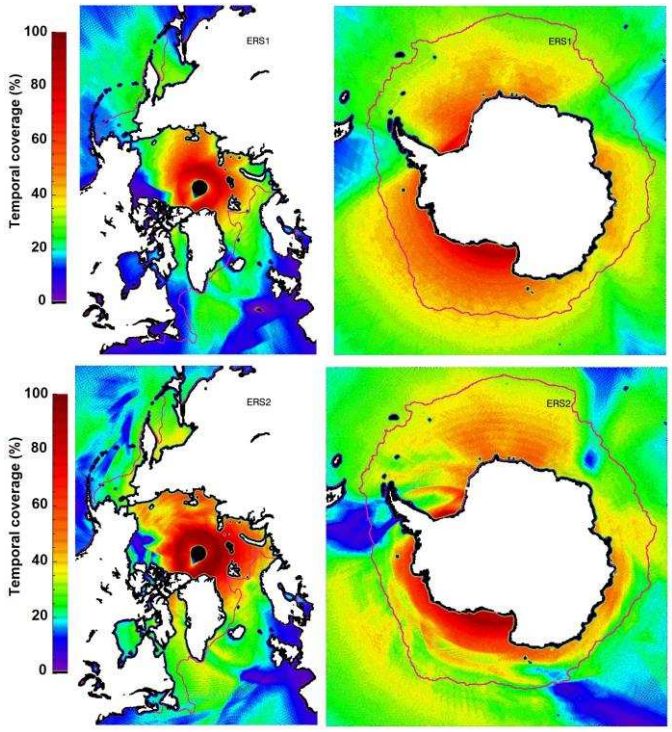

Fig. 4. ERS-1 (top panel) and ERS-2 (bottom panel) daily coverage in the Arctic (left) and Antarctic (right) with the winter sea ice edge displayed in pink. Daily coverage is defined as the number of updates per day. A daily coverage of 100% means that the pixel is updated daily - using observations from the previous 72 hours.

Indeed, in absence of observational input, the ERS sea ice extents will remain static on the prior from the previous day and unresponsive to change. Figure 4 displays the scatterometer daily coverage for the ERS-1 (1992-1996) and ERS-2 (1996-2000) missions, showing the areas that will likely be more affected by disruptions in the ERS data stream (when the wind mode is interrupted by SAR mode operations). During the ERS-1 period, extended areas around the Beaufort Sea, the Hudson Bay, and the Labrador Sea have a lower daily coverage than expected by symmetry. Smaller problems persist in the Beaufort Sea during ERS-2 period. In the Southern hemisphere, the western side of the Antarctica Peninsula has a lower than average daily coverage during ERS-2 period. Because of delays in the arrival of observational updates, the ERS sea ice extents over these regions are more likely to suffer from small negative (resp. positive) biases during the growth (resp. melt) season, and caution should be exercised in their analysis.

With the inclusion of ERS data, the scatterometer record of daily sea ice extents (built from QuikSCAT and ASCAT data) is extended to the period spanning from 1992 to 2000 as shown on Figure 5.

The next section describes the development of a sea ice backscatter model for ERS and ASCAT to produce a uniform sea ice backscatter record along with this new sea ice extent record.

IV. Sea Ice Backscatter Model at C-Band

The ERS and ASCAT scatterometers collect backscatter from a wide range of incidence angles, allowing the empirical characterization of the monostatic sea ice backscattering cross-section as a function of incidence angle and sea ice type. This characterization is required to normalize the backscatter maps to a single incidence angle, θ_0, and is valuable as an aid to theoretical studies of sea ice scattering. An empirical model for normalizing backscatter as a function of incidence angle is necessary to homogenize the backscatter records collected from instruments that observe many and different incidence angles (e.g. ERS and ASCAT), and a prerequisite to study long-term trends. Backscatter at one incidence is also used to typify the geophysical state of sea ice as seen with a C-band scatterometer at all angles. To develop such an empirical model, $\sigma^0_{ice}[\theta, \sigma^0_{ice}(\theta_0)]$, we need to transform the formulation of the sea ice GMF defined in Eq. (3), as expressed in terms of the WVC-dependent ice line parameters (α, β), into a formulation for the derivative of sea ice backscatter with incidence angle. Different sets of ice line parameters are used for Arctic and Antarctic sea ice in order to account for their different development characteristics. It is known that

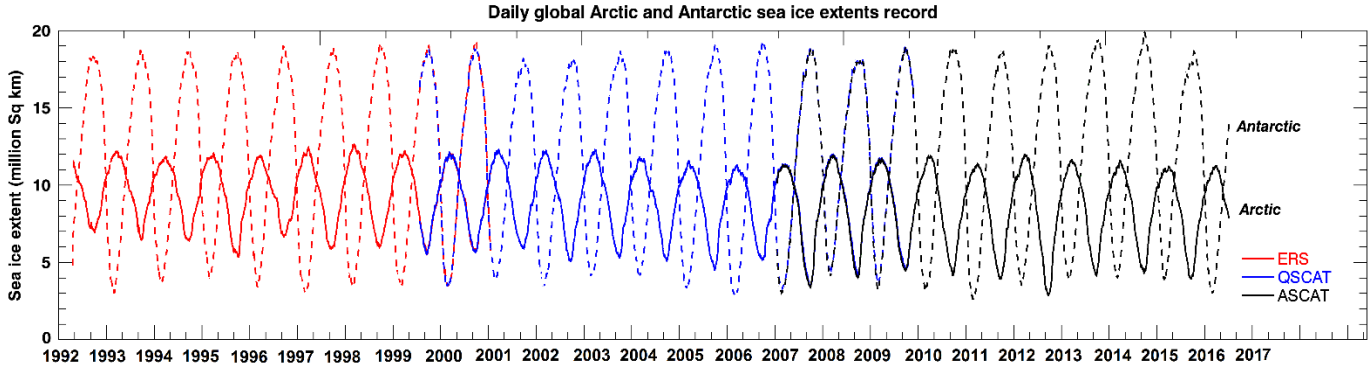

Fig. 5. Sea ice extent record from ERS-1, ERS-2, QuikSCAT and ASCAT data. The solid line represents the Arctic sea ice extent and the dashed line the Antarctic sea ice extent.

Antarctic sea ice is in general younger (more seasonal) and rougher (subject to more dynamic wave action) than Arctic sea ice, which is in turn less saline and more porous by virtue of its older age. These contrasting growth conditions, along with the underlying dominance of surface vs. volume scattering mechanisms, justify our use of hemisphere-dependent parameters to represent their backscatter derivatives.

The sea ice backscatter derivative over a given across-track WVC can be approximated from Eq. (3) as:

$$\left.\frac{d\sigma^0_{ice}}{d\theta}\right|_{\theta} \approx \frac{\sigma(\theta_{FORE}) - \sigma(\theta_{MID})}{\theta_{FORE} - \theta_{MID}} = -\frac{\alpha + (\beta - 1)\sigma^0_{FORE}}{\theta_{FORE} - \theta_{MID}} \quad (10)$$

where this quantity is evaluated at the mean incidence angle that corresponds to the across-track WVC:

$$\theta = (\theta_{MID} + \theta_{FORE})/2$$

Similarly, the side beam backscatter can be expanded as:

$$\sigma^0_{FORE} = \sigma^0_{ice} + \left.\frac{d\sigma^0_{ice}}{d\theta}\right|_{\theta_0} (\theta_{FORE} - \theta) \quad (11)$$

From (10) and (11), the sea ice backscatter derivative with incidence angle can now be expressed in closed form as:

$$\frac{d\sigma^0_{ice}}{d\theta} = A(\theta) + B(\theta) \cdot \sigma^0_{ice} \quad (12)$$

We see that it depends linearly on backscatter (i.e., sea ice type) with incidence dependent coefficients $A(\theta)$ and $B(\theta)$:

$$\begin{cases} A(\theta) = \dfrac{-2\alpha}{(1+\beta)(\theta_{FORE} - \theta_{MID})} \\ B(\theta) = \dfrac{-2(\beta - 1)}{(1+\beta)(\theta_{FORE} - \theta_{MID})} \end{cases} \quad (13)$$

The incidence dependent coefficients $A(\theta)$ and $B(\theta)$ are estimated for each hemisphere from the WVC-dependent iceline parameters (α, β) derived from the ERS and ASCAT wintertime distributions of sea ice backscatter, which generally fit the iceline to within 0.4 dB (1σ). To straddle the combined ERS and ASCAT incidence angle domains from 18° to 64°, smooth interpolating functions for the Northern and Southern Hemispheres are introduced:

$$\begin{aligned} A_{NH}(\theta) &= 0.257 - 0.00605 \cdot \theta \\ B_{NH}(\theta) &= 0.004 + 0.169 \cdot \exp(-0.075 \cdot \theta) \end{aligned} \quad (14)$$

$$\begin{aligned} A_{SH}(\theta) &= -0.397 + 0.01314 \cdot \theta - 0.0001310 \cdot \theta^2 \\ B_{SH}(\theta) &= 0.007 + 0.797 \cdot \exp(-0.206 \cdot \theta) \end{aligned} \quad (15)$$

Eq. (12) and the coefficients in Eqs. (14-15) above describe how the sea ice backscatter derivative at C-band changes with sea ice type, with darker sea ice types showing more negative slopes than older and more deformed sea ice types, and with incidence angle, with all ice types showing steeper negative slopes at lower incidences (see Fig. 6). The model thus characterizes the transition from a dominance of surface scattering effects for younger ice types and lower incidences, to volume scattering effects for older ice types and larger incidences [13]. The inhomogeneous first order differential equation for the sea ice backscatter derivative in Eq. (12) also admits an integral solution of the form:

$$\sigma^0_{ice}(\theta) = \sigma^0_{ice}(\theta_0) + \int_{\theta_0}^{\theta} u(\theta')A(\theta')d\theta' \quad (16)$$

$$u(\theta') = \exp\left(-\int_{\theta_0}^{\theta'} B(\theta'')d\theta''\right)$$

where the sea ice backscatter at some reference incidence $[\sigma^0_{ice}(\theta_0)$, which we take as proxy for sea ice type], acts as a boundary condition in the reconstruction of the monostatic C-band sea ice backscatter profile (see Fig. 7).

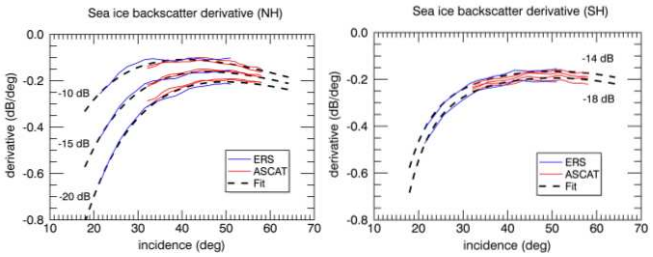

Fig. 6. Sea ice backscatter derivatives at C-band for the Northern Hemisphere (left) and Southern Hemisphere (right) for different background sea ice types (-10 to -20 dB)

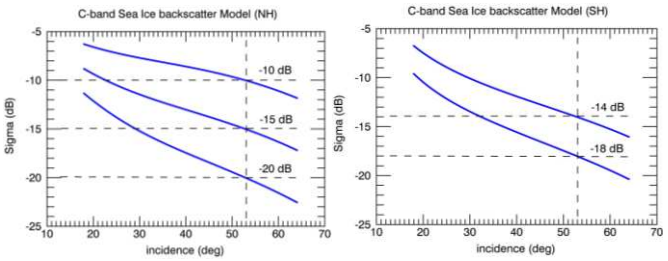

Fig. 7. Empirical C-band VV backscatter model for Arctic (left) and Antarctic (right) sea ice types (-10 to -20 dB at θ_0 = 52.8 degrees)

Note the different behaviour for the Arctic and Antarctic sea ice classes, particularly with regards to the location of the inflection point on the backscatter curve, which is related to the onset of volume scattering contributions and is found at much lower incidences in the Arctic. Figures (6-7) show that the relation between sea ice backscatter and incidence angle deviates slightly from linearity, and that the usual incidence angle correction described as a linear function of incidence with a slope depending on sea ice type [14-16] (which is equivalent to a shift-and-scale of backscatter histograms collected from different WVCs) may introduce errors in the location of the sea ice modes of up to 0.4 dB in the reduced range of ASCAT incidences (from 30 to 60 degrees) and of up to 1 dB when using the extended range of ERS and ASCAT incidence angles (18 to 63 degrees). Figures (8-9) illustrate the use of the C-band sea ice backscatter model developed in this paper as an incidence angle correction tool for both ERS and ASCAT data. Before normalization, the sea ice backscatter histograms feature several modes revealing the presence of dominant sea ice classes (i.e., dark modes for seasonal sea ice, and brighter modes for deformed and perennial sea ice types) spread over the backscatter domain as a function of WVC geometry. Note that, aside from the remarkable loss observed from 2000 to 2008 in the population of the bright ice mode observed at -14 dB, the C-band sea ice

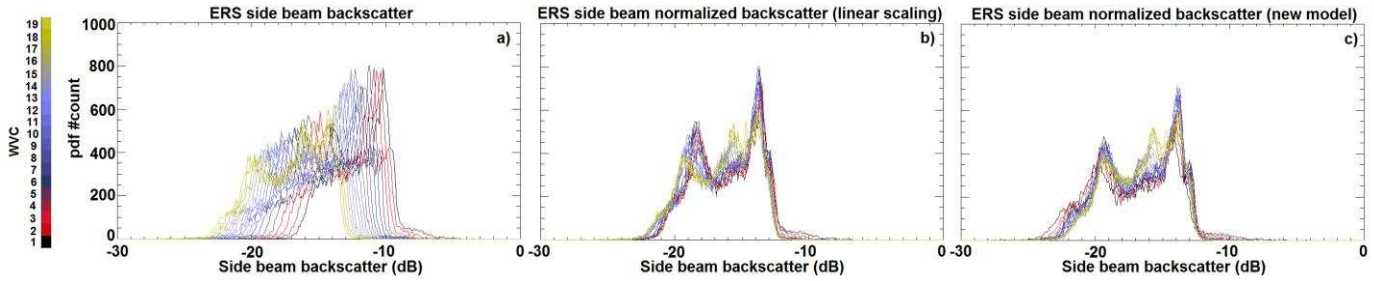

Fig. 8. Sea ice backscatter histograms collected by ERS in March 2000 over the Northern hemisphere: a) as a function of WVC, b) Normalized to 52.8° with linear scaling, c) Normalized to 52.8° with the model proposed in this paper

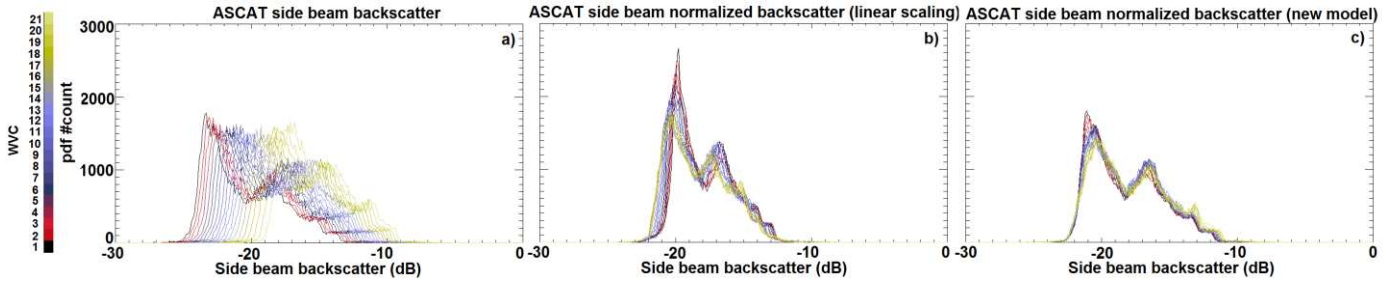

Fig. 9. Sea ice backscatter histograms collected by ASCAT in March 2008 over the Northern hemisphere: a) as a function of WVC, b) Normalized to 52.8° with linear scaling, c) Normalized to 52.8° with the model proposed in this paper

backscatter model developed in this paper performs better than the linear scaling at aligning the modes of each distribution, and succeeds at reproducing the increasing dynamic range between the Arctic seasonal and perennial sea ice modes with incidence angle. One potential limitation of the empirical sea ice backscatter model developed here is that it assumes a one-to-one relationship between C-band backscatter (collected at some reference angle) and sea ice type, which is not strictly correct, since we know that the backscatter signatures of deformed FY and second year ice can overlap to some degree. The distinction between rough FY and older sea ice types at C-band based on the characterization of the backscatter derivative should be examined further, but remains out of the scope of this work.

V. Summary and Conclusions

In this paper, an existing Bayesian sea ice detection algorithm for ASCAT is modified to discriminate sea ice from open water using observations collected by the scatterometers on board the European Remote Sensing satellites, ERS-1 and ERS-2. The sea ice extent record generated with the ERS scatterometer connects optimally with the QuikSCAT and ASCAT records to provide a consistent long-term dataset of scatterometer sea ice extents, albeit with a slightly lower quality because of its lower sampling rate. Still, the ERS sea ice record displays a characteristically better sensitivity to summer sea ice conditions than the passive microwave SSMI sea ice extents, a trait that all the scatterometer sea ice records appear to share. The Bayesian sea ice detection approach presented here has already been validated and applied towards the creation of QuikSCAT (1999-2009) and ASCAT (2007 to present date) sea ice extent records. The present work on ERS covers and completes the series of scatterometer sea ice extents from 1992 to 2001.

The ERS and ASCAT scatterometers collect sea ice backscatter measurements from a wide range of observation angles, allowing the characterization of the sea ice backscattering cross-section as a function of incidence and sea ice type. This empirical characterization is not only valuable from a theoretical point of view, but also necessary to normalize and homogenize the backscatter records collected from instruments that operate with a variety of observation angles. In this work, we have developed empirical models for Arctic and Antarctic sea ice backscatter at C-band VV-polarization based on the sea ice GMF derived from ERS and ASCAT observations. The proposed empirical C-band sea ice backscatter models demonstrate to be beneficial as a new normalization scheme (i.e., they are more accurate in the determination of sea ice backscatter modes than existing linear correction approaches), and realistic as far as the theoretical models go [13, 17, 18, 19]. The resulting histograms of normalized sea ice backscatter from the ERS and ASCAT records show remarkable changes in time, and should be further studied in order to consolidate the scatterometer capabilities to discriminate between seasonal, deformed and perennial sea ice types.

Acknowledgment

This work was supported by an educational grant from the ESA SCIROCCO project and has been made possible thanks to the support of the Satellite Observations Division of the Royal Netherlands Meteorological Institute. The authors are thankful to A. Verhoef for his helpful assistance during this work. The authors would like to thank EUMETSAT OSI SAF data support. The SSMI data were obtained from the NSIDC. The authors are grateful to the two reviewers for the time and attention dedicated to this manuscript and for their constructive comments.

REFERENCES

[1] Kurtz, N. T., Markus, T., Farrell, S. L., Worthen, D. L., and Boisvert, L. N., "Observations of recent Arctic sea ice volume loss and its impact on ocean-atmosphere energy exchange and ice production*", J.* Geophys. Res., vol. 116, no. C4, pp. 2156-2202, 2011.

[2] Comiso, J. C., "Large decadal decline of the Arctic multiyear ice cover", Journal of Climate, vol. 25, no. 4, pp. 1176-1193, 2011.

[3] Lindsay, R. and Schweiger, A., "Arctic sea ice thickness loss determined using subsurface, aircraft, and satellite observations", The Cryosphere, vol. 9, pp. 269-283, 2015.

[4] Belmonte Rivas, M. and Stoffelen, A., "New Bayesian algorithm for sea ice detection with QuikSCAT", IEEE Trans. Geosci. Remote Sens., vol. 49, no. 6, pp. 1894-1901, 2011.

[5] Belmonte Rivas, M., Verspeek, J., Verhoef, A., and Stoffelen, A., "Bayesian Sea Ice Detection with the Advanced Scatterometer ASCAT", IEEE Trans. Geosci. Remote Sens., vol. 50, no. 7, pp. 2649-2657, 2012.

[6] Drinkwater, M.R., Hosseinmostafa, R., and Gogineni, P., "C-band backscatter measurements of winter sea-ice in the Weddell Sea, Antarctica", International Journal of Remote Sensing, vol. 16, no. 17, pp. 3365-3389, 1995.

[7] Haarpaintner, J. and Spreen, G., "Use of enhanced-resolution QuikSCAT/SeaWinds data for operational ice services and climate research: sea ice edge, type, concentration, and drift", IEEE Trans. Geosci. Remote Sens., vol. 45, no. 10, pp. 3131-3137, 2007.

[8] Anderson, H.S. and Long, D.G., "Sea Ice Mapping Method for SeaWinds", IEEE Trans. Geosci. Remote Sens., vol. 43, no. 3, pp. 647-657, 2005.

[9] Stoffelen, A., Verspeek, J. A., Vogelzang, J., and Verhoef, A., "The CMOD7 Geophysical Model Function for ASCAT and ERS Wind Retrievals", IEEE J. Sel. Topics Appl. Earth Observ. Remote Sens., vol. 10, no. 5, pp. 2123-2134, 2017.

[10] Stoffelen, A. and Anderson, D., "Scatterometer Data Interpretation: Measurement Space and Inversion", J. Atmos. Oceanic Technol., vol. 14, pp. 1298–1313, 1997.

[11] Lin, W., Portabella, M., Stoffelen, A., Verhoef, A., and Turiel, A., "ASCAT wind quality control near rain", IEEE Trans. Geosci. Remote Sens., vol. 53, no. 8, 2015.

[12] Cavalieri, D. J., Parkinson, C. L., Gloersen, P., and Zwally, H., "Sea ice concentrations from NIMBUS-7 SMMR and DMSP SMM/I-SSMIS passive microwave data, version 1", Boulder, Colorado, USA, NASA National Snow and Ice Data Center Distributed Active Archive Center. Digital media, 2015.

[13] Firoozy, N., Mojabi, P., Landy, J., and Barber, D., "Landfast first year snow-covered sea ice reconstruction via electromagnetic inversion", IEEE Trans. Geosci. Remote Sens., vol. 9, no. 6, pp.2414-2428, 2016.

[14] Ezraty, R. and Cavanie, A., "Intercomparison of backscatter maps over Arctic sea ice from NSCAT and the ERS scatterometer", J. Geophys. Res., vol. 104, no. C5, pp. 11471-11483, 1999.

[15] Gohin, F. and Cavanie, A., "A first try at identification of sea ice using the three beam scatterometer of ERS-1", Int. J. Remote Sens., vol. 15, no. 6, pp. 1221-1228, 1994.

[16] Lindsley, R.D. and Long, D.G., "Enhanced resolution reconstruction of ASCAT backscatter measurements", IEEE Trans. Geosci. Remote Sens., vol. 54, no. 5, pp. 2589-2601, 2016.

[17] Drinkwater, M. R. and Crocker, G. B., "Modelling changes in the dielectric and scattering properties of young snow- covered sea ice at GHz frequencies", J. Glaciol., vol. 34, no. 118, pp. 274- 282, 1988.

[18] Barber D.G. and LeDrew, E.F., "Modelling synthetic aperture radar (SAR) scattering from a seasonally varying snow-covered sea ice volume at 5.3 and 9.25 GHz", Polar Research, vol. 13, no. 1, pp. 35-54, 1994.

[19] Fuller, M. C., Geldsetzer T, Gill, J. P. S., Yackel, J.J., and Derksen, C., "C-band backscatter from a complexly-layered snow cover on first-year sea ice", Hydrol. Process., vol. 28, no. 16, pp. 4614–4625, 2014.

Inès Otosaka received her M.Sc. degree in Environmental Engineering from the Royal Institute of Technology, Stockholm, Sweden, and her degree in Engineering from Ecole Centrale Marseille, Marseille, France in 2017. She conducted her master degree project at the Royal Netherlands Meteorology Institute (KNM) from September 2016 to March 2017.

She is currently working toward the Ph.D. degree in Earth and Environment at the University of Leeds, Leeds, United Kingdom.

Maria Belmonte Rivas received her B.Sc. degree in Earth Sciences from the Universidad Complutense de Madrid, Spain in 1999 and the M.Sc. and Ph.D. degrees in Physics and Aerospace Engineering from the University of Colorado in Boulder in 2007.

She is interested in the development of remote sensing techniques for Earth Observation. She has held positions at the European Space Agency (ESTEC, the Netherlands), the Colorado Center for Astrodynamics Research (CCAR) at the University of Colorado in Boulder (USA), the Atmospheric Chemistry Division at the National Center for Atmospheric Research (NCAR, Boulder, USA), and the Technical University of Delft (The Netherlands). She currently works at the Royal Netherlands Meteorology Institute (KNMI, The Netherlands).

Ad Stoffelen was born in 1962, in The Netherlands. He received his M.Sc. degree in physics from the Technical University of Eindhoven, Eindhoven, The Netherlands, in 1987 and the Ph.D. degree in Meteorology on scatterometry at the University of Utrecht, Utrecht, the Netherlands, in 1998.

He is working at the Royal Netherlands Meteorological Institute (KNMI) and responsible for the scatterometer wind products. He is also deeply involved in the European Space Agency ADM-Aeolus Doppler Wind Lidar mission. He currently leads a group on active satellite sensing at KNMI and is involved in topics from future missions and retrieval to 24/7 operations, user training and services.